Operational Modal Analysis of the Artemis I Dynamic Rollout Test and Wet Dress Rehearsal

James C. Akers[1], James P. Winkel[2], Alexander W. Chin[2], Russel A. Parks[3], Dana E. Chandler[3], Eric C. Stasiunas[3], and Matthew S. Allen[4]

[1] NASA Glenn Research Center
21000 Brookpark Road
Cleveland, Ohio 44135

[2] NASA Langley Research Center
1 Nasa Dr,
Hampton, VA 23666

[3] NASA Marshall Space Flight Center
4619 Beacon St SW,
Huntsville, AL 35812

[4] ATA Engineering,
13290 Evening Creek Drive S
San Diego, CA 92128

ABSTRACT

NASA has developed an expendable heavy lift launch vehicle capability, the Space Launch System (SLS), to support lunar and deep space exploration. The uncrewed Artemis I was the first flight of this new launch vehicle and tested critical systems for the upcoming crewed Artemis II flight to the moon. Accelerations were recorded at a multitude of locations on Artemis, the Mobile Launcher (ML), and the Crawler Transporter (CT)during the rollout of Artemis I from the Vehicle Assembly Building (VAB) to Launch Pad 39B March 2022 and is referred to as the Artemis I Dynamic Rollout Test (DRT). While Artemis I was at Launch Pad 39B, the Wet Dress Rehearsal (WDR) was performed to demonstrate launch readiness and acceleration measurements were also recorded. Finally, Artemis I rolled back from Launch Pad 39B to the VAB in April 2022, where acceleration measurements were also recorded and is referred to as the rollback portion of DRT.

Because the forces during rollout and at the launch pad acting on Artemis I, the ML, and the CT are not directly measurable, Operational Modal Analysis (OMA) techniques, instead of traditional Experimental Modal Analysis (EMA) techniques, were used to identify modal characteristics. The OMA analysis of DRT and WDR directly builds upon the lessons learned from the OMA analysis of an earlier rollout of the ML from the VAB.

DRT and WDR dynamic characteristics will be used to support SLS Integrated Modal Test finite element model correlation efforts and Exploration Ground System ML and CT finite element model verification and validation, which are part of the Building Block approach the Space Launch System program has implemented. The dynamic characteristics extracted from DRT as well as the rollout acceleration time histories themselves will be used in the development of generic rollout forcing functions that will provide refined estimates of the Artemis IV rollout forces, which will have the heavier and larger SLS Block 1B launch vehicle and Mobile Launcher 2 (ML-2).

This paper briefly describes Artemis I, the ML, and the CT physical characteristics, DRT rollout/rollback and WDR data collection, the challenges in implementing OMA techniques due in part to the CT harmonics, and how these challenges were overcome to obtain the Artemis I DRT configuration and WDR configuration modal characteristics.

Keywords: Artemis I, Operational Modal Analysis, NASA, Rollout, Space Launch System, Keyword Four

INTRODUCTION

While the rollout environment has historically produced relatively small launch vehicle structural loads for the National Aeronautics and Space Administration (NASA) Apollo and Space Shuttle programs in comparison to launch and ascent loads, these relatively small structural loads are inputs to structural fatigue analyses [1-5]. The same holds true for the Space Launch System (SLS) developed by NASA to support lunar and deep space exploration [6, 7]. Because the rollout forces are not directly measurable, Operational Modal Analysis (OMA) techniques, instead of traditional Experimental Modal Analysis (EMA) techniques, provides an empirical means to identify the integrated system rollout modal characteristics. OMA techniques were applied to the Artemis I Dynamic Rollout Test (DRT) and Wet Dress Rehearsal (WDR) test data to identify their fundamental modes during rollout and while on-pad, respectively. These identified modal characteristics will be used to assist in model correlation efforts and to better understand the rollout environment.

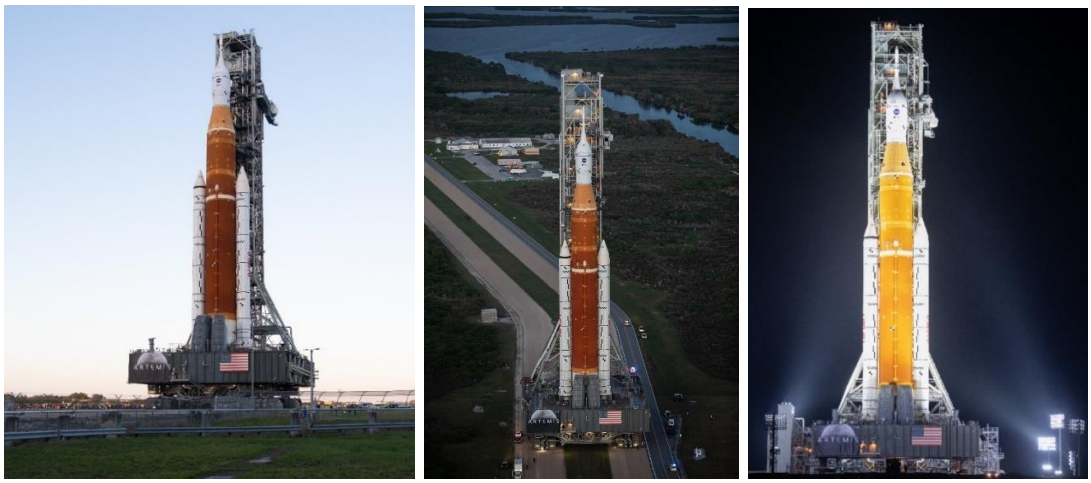

Figure 1. Artemis I rollout to Launch Pad 39B (left and center) and at launch pad (right)

The Artemis I DRT occurred in March 2022 (rollout) and April 2022 (rollback) and consisted of the Mobile Launcher (ML) being transported by the Crawler Transporter (CT-2) while transporting the Artemis I integrated vehicle from the VAB to Launch Pad 39B (rollout) and back to the VAB (rollback). The Artemis I integrated vehicle had the SLS Block I launch vehicle, which will also be used for Artemis II and Artemis III flights. Figure 1 shows the CT transporting Artemis I integrated vehicle on the ML out to Launch Pad 39B during DRT. When the CT is moving, below 15 Hz the primary excitation comes from the rollout ground forces generated by the CT with the major contributors being the impulsive forces generated by the CT Truck Tread Shoes making initial contact with the ground and when they pass under the CT Truck rollers. Lateral oscillations of the interim Cryogenic Propulsion Stage Umbilical (iCPSU) that are being driven by the rollout ground forces can be seen in the video of the Artemis I DRT rollout around 2:57:37 elapse time [8]. When the CT is stopped or when the ML and Artemis I integrated vehicle are at Launch Pad 39B, where the ML is being supported on the six large steel posts referred to as the Mount Mechanisms (MM), the primary excitation consists of wind loading on the ML Tower and the Artemis I integrated vehicle. The Wet Dress Rehearsal (WDR), which occurred between the DRT rollout and rollback, consisted of the ML being supported on the six MM at Launch Pad 39B. Figure 1 shows Artemis I integrated vehicle on the ML sitting at Launch Pad 39B during the WDR. In addition, when the ML was at Launch Pad 39B it was supported with four Extensible Columns positioned near the perimeter of the flame hole providing additional vertical support to the ML. Extensible Columns are not a new concept and were used to support the ML used for Apollo Saturn V launches. Figure 2 shows the Extensible Columns and the Side Flame Deflectors. Also at Launch Pad 39B, the ML was connected to the Ignition Over Pressure Sound Suppression (IOPSS) water supply piping. The IOPSS piping and particularly the Extensible Columns significantly change the dynamic characteristics of the ML from that seen inside the VAB where it is only supported on the six MM's.

Figure 2. Launch Pad 39B extensible columns and side flame deflectors

OMA assumes the system is linear time invariant and the excitation is broadband random in nature, spatially distributed, spatially uncorrelated, and stationary. There are three challenges with applying OMA techniques to the DRT Rollout and Rollback. The first challenge is the excitation is not broadband random in nature nor is it spatially distributed when the CT is moving. Instead, when the CT is moving the primary excitation is generated by the CT Trucks. The CT Trucks produce impulsive forces from their tracks, which produces vibration that transmit up through the CT into the ML and the Artemis I integrated vehicle. These impulsive force time histories form two sets of dominant harmonic excitations that manifest themselves as narrowband Gaussian random processes in the frequency domain. Harmonic excitation of a system can lead both the OMA time-domain and frequency-domain techniques to incorrectly identify a system harmonic response as true structural modes. If the CT harmonics were composed of sinusoidal excitations having nearly constant amplitudes and frequencies, current OMA harmonic reduction tools are well suited to remove them from the measured acceleration time histories and thus avoid this error. However, because the CT harmonics are narrowband Gaussian random processes, which lie in the frequency range of the fundamental modes, it is simply not possible to remove them without removing the signal content from the structural modes of the integrated system. The second challenge is the high modal density and many closely spaced modes. The rule of thumb for OMA analysis is that time histories having a duration of 1000 time periods of the lowest frequency mode are sufficient. Due to closely spaced modes, 1000 time periods may not be sufficient and significantly longer durations may be needed. The third challenge is the Artemis I DRT and WDR configurations have significant nonlinear characteristics, which is in part due to the Vehicle Stabilization System (VSS) that connects the upper portion of the SLS Core Stage to the ML Tower to stabilize and restrain the motion of Artemis I and the umbilicals.

The SLS program has implemented a Building Block approach [12 - 14] as part of its certification process for the Artemis I flight and in refining the Artemis I rollout forcing functions. As part of this, modal characteristics have been identified from the modal test of the ML [9, 10], which was performed in June 2019 inside the VAB, the ISVV-010 rollout of the ML on the CT from the VAB to Launch Pad 39B immediately following the ML Modal test [11], and the Integrated Modal Test (IMT) performed in September 2021 inside the VAB of the integrated Artemis I vehicle on the ML. It should be noted that for the IMT neither the umbilicals nor the VSS were deployed nor were there extensible columns or IOPSS. Hence the DRT and WDR modal dynamics characteristics are significantly different from those of the IMT and therefore provide important supplemental information to help reduce uncertainty in the test correlated Artemis I, ML, and CT Finite Element Models (FEM's) to achieve well test correlated FEM's that play a key role in the Building Block approach.

This paper will briefly describe the Artemis I DRT and WDR configurations, how Artemis I DRT and WDR data was collected, the challenges in implementing OMA techniques, and how these challenges were overcome to obtain the Artemis I DRT and WDR configuration modal characteristics.

Mobile Launcher and Crawler Transporter

The Mobile Launcher (ML) is a very large and heavy steel structure designed to support SLS during its buildup and integration inside the Vehicle Assembly Building (VAB), transportation from the VAB out to Launch Pad 39B, and provides the launch platform at Launch Pad 39B. The ML consists of the Tower and Base structures. The ML Tower is an open beam/truss steel structure weighs 4 million pounds, is 355 feet tall, and the upper levels are 40 square feet with floors every 20 feet for personnel access. The ML Tower provides lateral support to the integrated SLS launch vehicle via the Vehicle Stabilization System (VSS) and supports the fuel, power, and data umbilicals running to SLS and MPCV. The ML Tower

also provides crew access to the Orion Multi-Purpose Crew Vehicle (MPCV) Crew Module (CM) via the Crew Access Arm (CAA). The ML Base is a two-story structure 25 feet high, 165 feet long, 135 feet wide, weighing 6 million pounds. ML weighs approximately 10.6 million pounds and is over 380 feet tall [15]. ML Deck 0, the top surface of the ML Base, supports the SLS at eight attachment points located at the bottom of its two boosters via the ML Vehicle Support Posts (VSP). Figure 3 shows the layout of the ML umbilicals [16]. For the Artemis I DRT and WDR, the umbilicals and Vehicle Stabilizer System (VSS) were connected, but the CAA was retracted and rotated to the side of the ML Tower as shown in Figure 1.

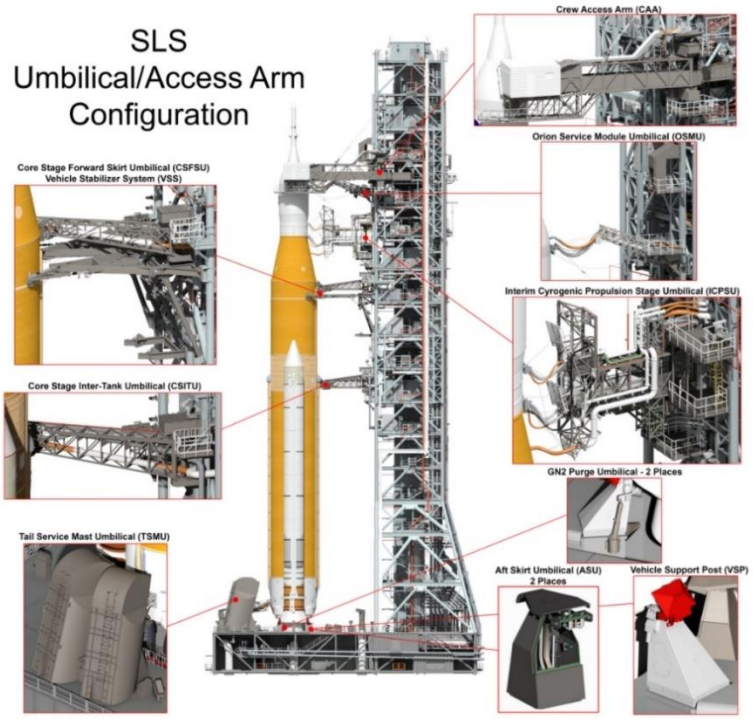

Figure 3. ML umbilicals (from http://NASASpaceFlight.com)

The Crawler Transporter (CT) performs all lifting and transport operations of both the rollout of the ML with the SLS integrated vehicle from the VAB to Launch Pad 39B and the rollback of the ML from Launch Pad 39B back into the VAB after launch. CT-2 is a recently upgraded version of one of the original CT's used for the Apollo and Space Shuttle programs [17 - 19] with their design based upon heavy mining machinery. These upgrades allow the CT-2 to carry the heavier loading imposed by the integrated SLS launch vehicle and ML. CT-2 is the size of a baseball infield, with a top speed of 1 mph loaded and 2 mph unloaded. CT-2 weights 6.3 million pounds total, height of between 20 feet and 26 feet depending on its jacking level. Jacking, Equalization, and Leveling (JEL) of the ML/SLS is performed by the JEL hydraulic system. Four hydraulic cylinders at each corner are pressurized by redundant pumps and provide for lifting and leveling control of the stack. The JEL's keep the stack level while negotiating the 5% incline of the ramp to Launch Pad 39B. The JEL's support the weight of the CT chassis, 2.2 million pounds, and the weight of the ML and SLS. For the Artemis I DRT the JEL's supported a total weight of 15.3 million pounds, 10.6 million pound ML, 2.2 million pound CT Chassis, and 3.5 million pound Artemis I integrated vehicle. The CT maximum load capacity is 18 million pounds. The CT provides vertical support for the ML at four (4) pickup points. Lateral mechanical constraints for the ML are provided at three of the four pickup points to minimize ML-to-CT support constraint stresses. Figure 4 is an aerial view of the CT-2 showing the four pickup points and the lateral mechanical constraints (yellow arrows) at each pickup point. These lateral mechanical constraints at each pickup point are designed to provide a lateral kinematic connection between the ML and CT so that ML does not impart static lateral loads into the CT and vice versa. Because of this Corner B has no lateral mechanical constraints. However, accelerometers mounted on the ML and CT sides of these ML/CT pickup points shows that friction prevents slipping from occurring when the CT is transporting the ML.

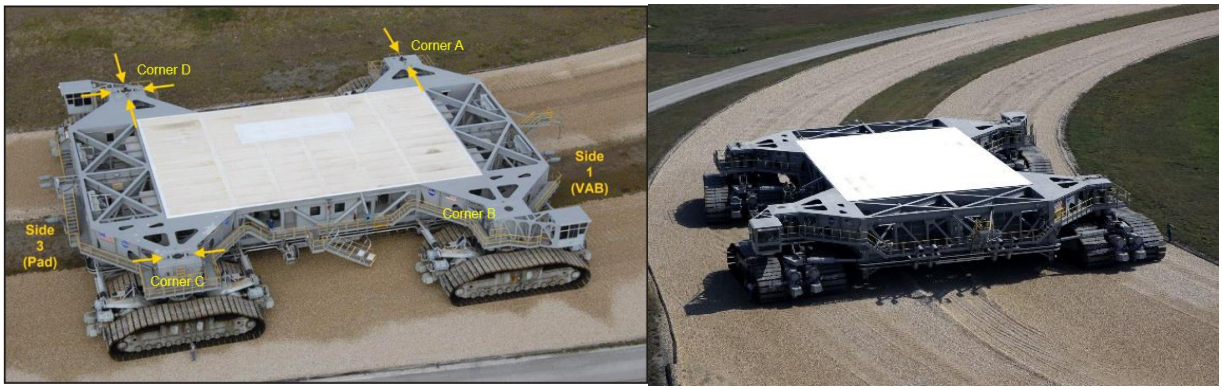

Figure 4. Aerial view of CT-2 showing pickup points [5]

The CT has four trucks, each having two tracks. Each CT truck weighs approximately 1 million pounds. Each track has 57 shoes with each shoe weighing 2,100 lb. Each track is driven by two 375 hp electric motors (four per truck) that are powered by four 1,000 kW DC generators that in turn are powered by two Alco 16 cylinder diesel engines. While the CT's internal drive train gearing does produce harmonic excitations, the most significant harmonic excitations are generated by the truck tracks and rollers [2]. One set of dominant harmonics is due to the initial slap of the track shoes making contact with the ground, referred to as the shoe slapping harmonics, which are a function of CT speed and shoe spacing. Another set of dominant harmonics is due to the track shoes passing underneath the 11 support rollers of each truck, referred to as the roller crossing harmonics, which are also a function of the CT speed and the spacing between the support rollers. The amplitude of these track shoe and roller crossing harmonics is also a function of CT speed, with the amplitudes increasing with increasing CT speed. The Crawlerway, the 40 foot wide 4.2 mile long prepared surface the CT traverses between the VAB and Launch Pad 39B, underwent repair 2013- 2014 timeframe to prepare the Crawlerway to be able support the transport of SLS [20]. The physical characteristics of the Crawlerway directly affect the reaction forces generated by the CT Trucks. The Crawlerway can handle weights of up to 26 million pounds. It takes the CT approximately 8 hours to transport the ML or the ML with SLS on it between the VAB and Launch Pad 39B.

Figure 5 shows the CT truck tracks and Figure 6 shows the relationship between these CT harmonics and the Artemis I DRT configuration fundamental modes. Note that these CT harmonics are dispersed within the frequency range of these fundamental modes. Although the harmonic frequencies of these two sets of CT harmonics remain relatively constant for a constant CT speed, the continuous variations due to the shoes not engaging all rollers, variations in the amplitudes and relative phasing between the impulsive CT shoe forces, and variation in the Crawlerway surface results in the CT harmonics manifesting themselves in the frequency domain as narrowband Gaussian random processes (i.e., kurtosis close to 3). This makes it very challenging to model analytically and to remove the effect of these CT harmonics. Figure 7 shows the CT speed profiles during both the DRT rollout and rollback. Note that the CT does not turn around, but simply drives in reverse when traveling from Launch Pad 39B back to the VAB, hence the CT speeds during the DRT rollback are negative. All times are given with respect to the Eastern Daylight Savings Time (EDT) time zone.

Figure 5. CT during ISVV-010 rollout June 2019 (left) and rollout conducted September 2019 (right)

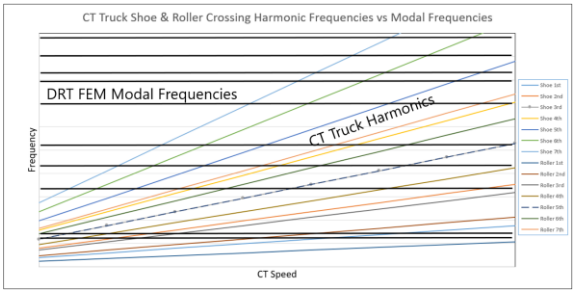

Figure 6. CT truck track shoe and roller first seven harmonic frequencies vs Artemis I DRT FEM fundamental modal frequencies

ARTEMIS I DRT AND WDR INSTRUMENTATION

For the Artemis I DRT and WDR, data from of over 300 accelerometers located on Artemis I, ML, and CT was recorded on two independent data acquisition systems (DAQ's), the SLS Mobile Data Acquisition System (MDAS) and the accelerations on the CT channels were acquired with the CT Data Acquisition System (CTDAS). Accelerations on Artemis I and the ML were recorded on MDAS. The accelerometers on Artemis I were a subset of those used during the Integrated Modal Test, specifically accelerometers were removed from the aft end of the Core Stage in the Engine Section area due to scheduling constraints. In addition, CTDAS recorded 4 CT JEL pressures (one at each truck) and CT Speed. The anemometer data collected at the top of the ML Tower (i.e., wind speed and wind direction with respect to ML orientation) was recorded with the independent Sensor Data Acquisition System (SDAS). SDAS also recorded the permanently installed instrumentation that included accelerometers and strain gages whose purpose is to measure responses during prelaunch and liftoff. This set of accelerometers was not assessed in this OMA analysis because it had been previously found from the OMA analysis of the ISVV-010 rollout that these accelerometers did not have sufficient sensitivity nor low enough sensor noise level.

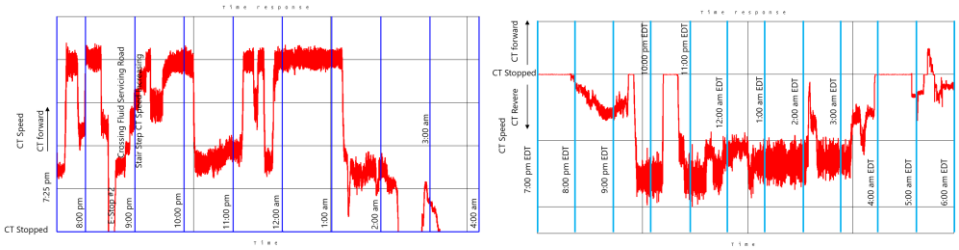

Figure 7. Artemis I DRT CT speed profiles: rollout (left) and rollback (right) (EDT time zone)

The MDAS, CTDAS, and SDAS had different sampling frequencies and were not time synchronized. The MDAS and CTDAS sampling frequencies were significantly higher than required to identify the target modes and resulted in very large data files that were challenging to handle and analyze. Figure 8 shows the test display model (TDM) with the locations and orientation of the ML and CT accelerometers used to animate the OMA identified test mode shapes and the Artemis I DRT FEM. The Artemis I WDR TDM is the same as the Artemis I DRT TDM except the CT portion has been removed. It has become increasingly popular to partially back expand test mode shapes to a larger set of grid points or even to the full FEM. Caution should be exercised when doing so because small errors in the test mode shapes, due to ambient noise, sensor noise, and nonlinearities in the test article, combined with differences between the FEM and the test hardware, which produces errors in the back expansion matrix. These back expanded mode shapes can lead to erroneous local deflections in the back expanded test mode shapes that can mislead their interpretation and FEM correlation efforts. If the animation of the test mode shapes back expanded so there are only all three translational degrees of freedom (DOF) at each instrument location is insufficient for the test engineer to visually interpret them, then it is recommended the instrumentation set be revised. The TDM shown in Figure 8 only has grid points located where accelerometers were mounted and consisted of triangular plate elements and trace lines. Triangular plate elements were used to connect adjacent grid points to provide depth of field to help

with visualizing mode shapes. Note that the shading of the triangular plate elements could be turned off if a purely "trace line" type of TDM is desired.

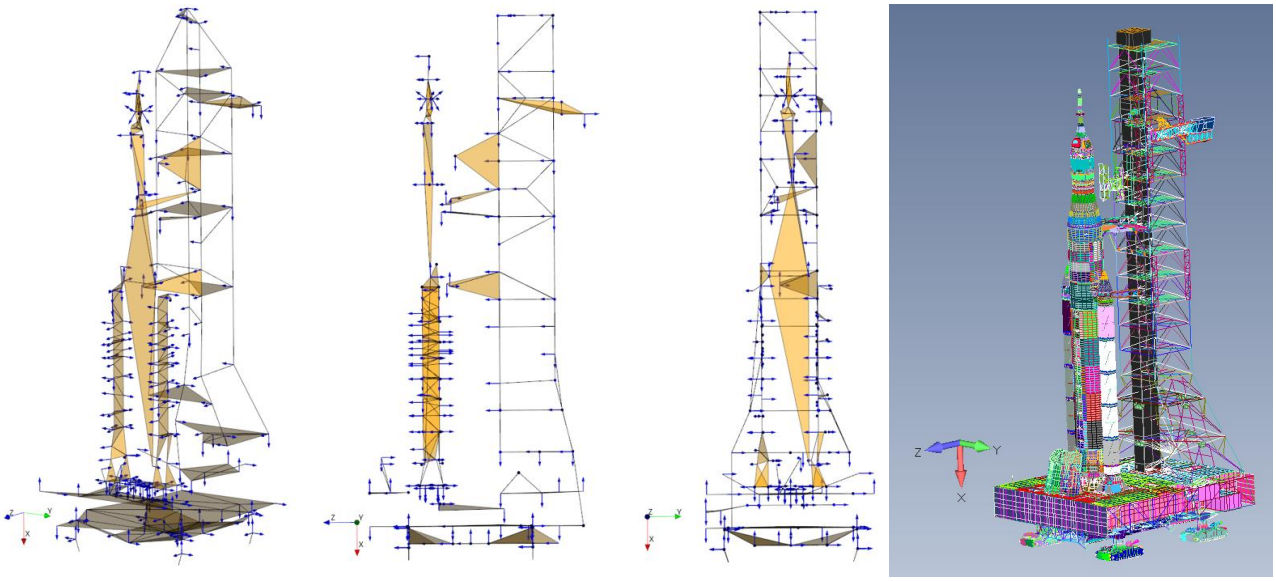

Figure 8. Artemis I DRT TDM (left) and FEM (right)

PREVIOUS OMA ANALYSIS OF ROLLOUTS

The Artemis I DRT and WDR OMA analysis built upon experience gained in applying OMA techniques to the ISVV-010 rollout (ML transported by CT) in June 2019, CT-2 unloaded and rollouts with the Space Shuttle Mobile Launcher Platform (MLP) in March 2017, Space Shuttle CT unloaded and rollouts with the MLP in February 2005, and the Partial Stack rollout (space Shuttle CT transporting an MLP with two solid Rocket Boosters connected with a thrust beam at their forward attachment fittings) in November 2003 [11, 21]. Figure 9 shows the ML on CT during the ISVV-010 roll out of the VAB.

Figure 10 shows the Shuttle-era CT transporting the Space Shuttle on the MLP and the Partial Stack rollout configuration. Figure 11 shows the Shuttle-era CT transporting the MLP. MLP did not have a launch tower structure like the current ML, but instead there was the Rotating Service Structure (RSS) at the launch pad [22 - 24]. The RSS provided protected access to the orbiter for installation and servicing of payloads at the Launch Pads 39A and B, as well as servicing access to certain systems on the orbiter. The RSS can be seen in the far left of Figure 11.

Figure 9. ISVV-010 rollout, ML on CT leaving VAB at midnight June 28

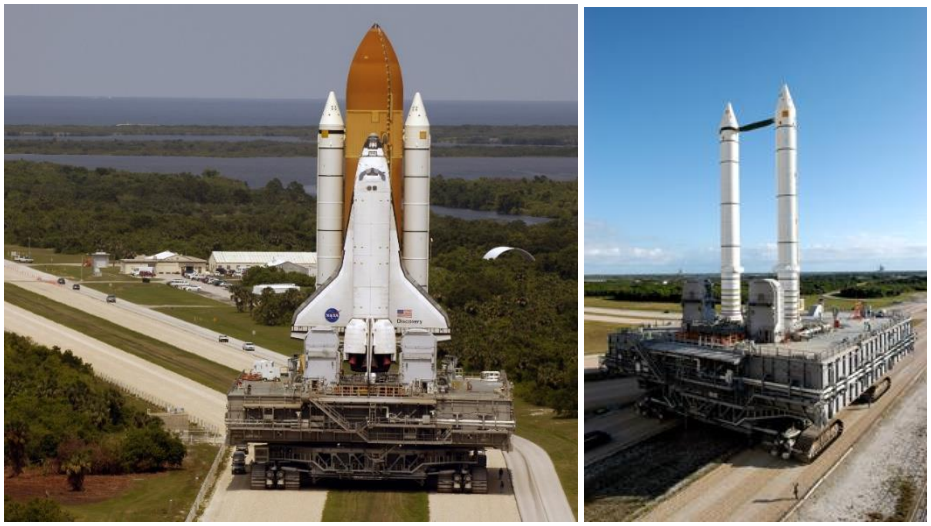

Figure 10. Shuttle-Era CT transporting Space Shuttle on the MLP (left), Partial Stack Rollout (right)

Figure 11. Shuttle-Era CT transporting MLP

ARTEMIS I DRT AND WDR FEM

The Artemis I DRT FEM consisted of 17 different superelement components that needed to be assembled into a single residual run along with physical representations of the ML, CT, MPPU, and various parts of the SLS stack. The total weight of the Artemis I DRT FEM was 21.5 million pounds. The approximate weight breakdown was the CT, ML, and all associated hardware weighed 18 million pounds the unfueled SLS stack weighed about 3.5 million pounds primarily due to the two boosters.

There are many benefits to having a FEM and the associated Test Analysis Model (TAM) prior to any modal testing effort. For an OMA testing effort however, it's importance cannot be understated. It is critical for OMA analysis to help focus modal parameter identification efforts to help ensure that all target modes are identified. In addition, the TAM mass matrix allows for comparisons of test and FEM mode shapes using a cross-orthogonality criteria and comparisons of test shapes to themselves using a self-orthogonality criteria [25]. Finally, the TAM backexpansion matrix allows test shapes to be back expanded to all three translational DOF at each instrument location, which tremendously aids in visual interpretation of test mode shapes. Figure 8 shows the Artemis I DRT FEM. It is beneficial to have the FEM pass all standard modeling checks to verify no modeling errors have been made.

Target modes were selected based upon modal effective mass which showed that all significant mass driving modes occurred below 6 Hz. The selection criteria of primary or secondary target modes were made by utilizing a combination of visual inspection, the modal effective mass fractions, the element strain energy distribution, and the grid point kinetic energy distribution. Figure 12 shows the modal effective mass and target mode selection for the first 30 Artemis I DRT FEM

modes. The strain energy distribution and grid point kinetic energy distribution were both reviewed by dividing the FEM elements and grids into groups of major components, respectively. This allowed a detailed distribution per mode to be displayed making it easy to determine which components were the primary drivers in each mode. Figure 13 shows the element strain energy and Figure 14 shows the grid point kinetic energy by component group for the first 30 Artemis I DRT FEM modes. In some cases, like mode 26, the element strain energy is almost all located in one of the superelements and thus the total sum will not add up to 100%.

Mode #	Target Mode	MEFF Table T1	T2	T3	R1	R2	R3	Description
1	P1	0%	0%	29%	0%	8%	0%	Z Stack Bending
2	P2	0%	31%	0%	14%	0%	10%	Y Stack Bending
3	P3	0%	2%	0%	5%	0%	3%	Y SLS Bending
4	P4	0%	0%	3%	0%	3%	0%	Z SLS Bending
5		0%	0%	0%	0%	0%	0%	MPCV SM Tank Slosh
6		0%	0%	0%	0%	0%	0%	MPCV SM Tank Slosh
7		0%	0%	0%	0%	0%	0%	MPCV SM Tank Slosh
8		0%	0%	0%	0%	0%	0%	MPCV SM Tank Slosh
9	P5	0%	0%	0%	2%	0%	0%	SLS Torsion
10	P6	0%	0%	2%	0%	2%	0%	LAS Z First Bending
11	P7	0%	0%	0%	1%	0%	1%	LAS Y First Bending/In Phase Tower Torsion
12	P8	0%	0%	0%	1%	0%	0%	LAS Y First Bending/Out of Phase Tower Torsion
13	P9	0%	0%	0%	0%	0%	0%	SLS Axial Mode/SRB Bending Out of Phase
14	S1	0%	0%	11%	0%	10%	0%	Tower Z 2nd Bending
15	S2	0%	27%	0%	20%	0%	26%	Tower Y 2nd Bending/CSITU Rigid Body Rotation
16	S3	0%	0%	0%	0%	0%	0%	ICPSU Rigid Body Rotation out of phase with CSITU and CSFSU Rigid Body Rotation
17	S4	0%	1%	1%	0%	1%	1%	CSITU Bending and Rotation
18	P10	1%	0%	8%	0%	8%	0%	SLS 2nd Bending Z /SRB Bending Out of Phase with Core Stage
19	P11	0%	3%	0%	1%	0%	4%	SLS 2nd Bending Y/SRB Bending Out of Phase with Core Stage
20	S5	0%	1%	0%	0%	0%	1%	CSFSU Rigid Body Rotation
21	P12	10%	0%	2%	0%	1%	1%	CSITU 1st Bending Vertical/SLS 2nd Bending Z In Phase
22	P13	0%	0%	1%	0%	1%	0%	CSITU 1st Bending Vertical/SLS 2nd Bending Z Out of Phase
23	S6	15%	7%	0%	5%	0%	8%	Tower 2nd Bending Y/SLS 2nd Bending Y/CSITU and CSFSU Vertical Bending Out of Phase
24	P14	20%	7%	0%	4%	0%	8%	Tower 2nd Bending Y/SLS 2nd Bending Y/CSITU and CSFSU Vertical Bending Out of Phase
25	P15	0%	1%	0%	3%	0%	2%	SLS 3rd Bending Y
26		0%	0%	0%	0%	0%	0%	ICPS Engine Mode
27		3%	0%	4%	0%	4%	0%	CSFSU Vertical Bending
28	P16	1%	1%	1%	0%	1%	1%	CAA Torsion / SLS Torsion
29	P17	17%	0%	14%	0%	19%	0%	CT Rocking Z/Tower 3rd Bending Z/SLS Torsion
30	S7	2%	0%	1%	0%	1%	0%	CAA Torsion

= Primary Target Mode
= Secondary Targt Mode
Modal Effective Mass ≥ 10%
Modal Effective Mass ≥ 1%, but < 10%

Figure 12. Artemis I DRT FEM modal effective mass for first 30 modes

Mode Number	1	2	3	4	5	6	7	8	9	10	11	12	13	14	15	16	17	18	19	20	21	22	23	24	25	26	27	28	29	30
CT	8%	11%							9%					9%	23%			9%			8%		16%	18%			9%		29%	
MLBase	32%	14%	7%	8%					9%					10%	23%			11%	6%		7%		16%	17%					11%	
EngineServicePlatform																														
TSMU																														
MPPU																														
MLTower	50%	55%	22%	12%					5%		37%	44%		77%	47%	82%	65%	7%	12%	68%	21%	20%	38%	35%	6%		29%	14%	34%	25%
CSITU																	26%				20%	34%	9%							
VSS			16%	50%					6%		8%																			
CSFSU																			26%				7%				48%			
ICPSU																9%														
CAA																												23%		40%
CoreStage		7%	23%	8%					27%	40%	24%	13%	10%						12%		8%	10%			13%			19%		9%
LEFT_SRB		6%	14%	7%					27%				42%					22%	30%					6%				13%	12%	7%
Right_SRB		6%	14%	7%					26%	5%			42%					23%	30%				5%					20%		9%
LVSA										10%	8%	7%																		
ICPS										7%	5%																			
MSA																														
MPCV					99%	100%	100%	97%		15%	8%	8%						13%			24%	21%		7%	50%					15%
CNXN_LeftSRB_ML																														
CNXN_RightSRB_ML																														
CNXN_LeftSRB_CoreStage																														
CNXN_RightSRB_CoreStage																														
CNXN_LVSA_CoreStage																														
CNXN_ICPS_LVSA																														
CNXN_MSA_ICPS																														
CNXN_MPCV_MSA																														
Total	100%	100%	97%	97%	100%	100%	100%	100%	99%	96%	98%	97%	99%	100%	100%	100%	100%	95%	99%	100%	94%	94%	99%	98%	86%	4%	100%	99%	100%	99%

5% ≤ ESE < 25%
25% ≤ ESE < 50%
ESE ≥ 50%

Figure 13. Artemis I DRT FEM element strain energy for first 30 modes

The instrumentation set (i.e., test DOF) used for the Artemis I DRT and WDR were not specifically selected for these configurations, but instead used a subset of the instrumentation sets used for the IMT that was performed in September 2021. Accelerometers were removed from the engine sect at the aft end of the SLS Core Stage to facilitate schedule constraints. Also for the IMT, the umbilicals and VSS were not in their deployed configurations as they were for Artemis I DRT and WDR. Even with these limitations, the pseudo-orthogonality and self-orthogonality of the Artemis I DRT FEM target modes showed the instrumentation set did a good job of adequately separating most target modes (i.e., most off-diagonal values less than 10%) [25]. Figure 15 shows the pseudo-orthogonality and self-orthogonality for the first 24 Artemis I DRT FEM target modes. Besides assessing the pseudo-orthogonality and self-orthogonality of just the target modes, the pseudo-orthogonality and self-orthogonality of all modes in the frequency range of the target modes should also assessed since this is what the test

engineer will see during testing. Figure 16 shows the pseudo-orthogonality and self-orthogonality for the first 30 Artemis I DRT FEM modes, which encompasses the first 24 target modes. There was no instrumentation to capture propellant sloshing in the MPCV Orion Service Module (SM) propellant tanks nor on the iCPS RL-10 engine bell to capture its rocking. As expected, the pseudo-orthogonality and self-orthogonality of all modes broke down in these frequency regions (e.g., propellant slosh and the iCPS RL-10 engine bell rocking look similar to lateral bending modes). As expected, due to this lack of instrumentation the slosh modes have diagonal values less than 1% in the pseudo-orthogonality and the self-orthogonality has off-diagonal values greater than 90% (i.e., Artemis I is bending with the SM propellant tanks sloshing in-phase and out-of-phase). The test engineer when identifying modes should keep these limitations in mind, which may manifest themselves as multiple mode shapes closely spaced in frequency that are nearly indistinguishable (e.g., SM slosh modes will all appear to be 1st lateral bending).

Mode Number	1	2	3	4	5	6	7	8	9	10	11	12	13	14	15	16	17	18	19	20	21	22	23	24	25	26	27	28	29	30
CT																														
MLBase															16%						6%		18%	19%			8%		22%	
EngineServicePlatform																														
TSMU																														
MPPU																														
MLTower	73%	68%	25%	18%							23%	27%		86%	71%	14%	7%		11%	9%	15%		40%	42%	6%		10%	5%	35%	10%
CSITU																11%	76%				32%	53%	13%							
VSS																														
CSFSU																8%	6%			79%			8%	11%			70%		7%	
ICPSU											10%	16%				62%	5%													
CAA											5%	6%																31%		55%
CoreStage				6%														8%	9%											
LEFT_SRB	7%	11%	32%	31%					47%	7%			50%					29%	36%				7%					22%	17%	11%
Right_SRB	7%	11%	32%	31%					46%	8%			50%					29%	36%				6%					30%	6%	14%
LVSA																														
ICPS																										6%	96%			
MSA																														
MPCV				11%	99%	100%	100%	97%		80%	48%	40%						19%			36%	33%	6%	11%	68%					
CNXN_LeftSRB_ML																														
CNXN_RightSRB_ML																														
CNXN_LeftSRB_CoreStage																														
CNXN_RightSRB_CoreStage																														
CNXN_LVSA_CoreStage																														
CNXN_ICPS_LVSA																														
CNXN_MSA_ICPS																														
CNXN_MPCV_MSA																														
Total	100%	100%	100%	100%	100%	100%	100%	100%	100%	100%	100%	100%	100%	100%	100%	100%	100%	100%	100%	100%	100%	100%	100%	100%	100%	100%	100%	100%	100%	100%

5% ≤ GKE < 25%
25% ≤ GKE < 50%
VKE ≥ 50%

Figure 14. Artemis I DRT FEM grid point kinetic energy for first 30 modes

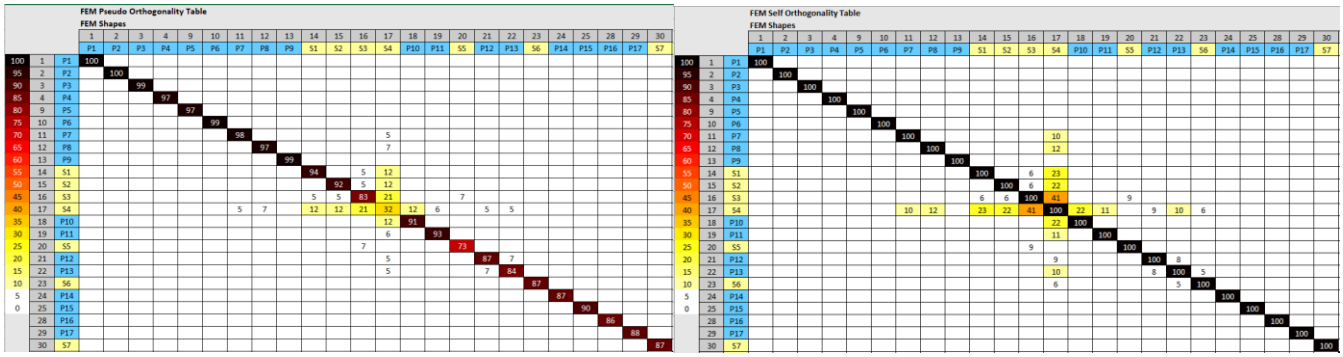

Figure 15. Artemis I DRT FEM first 24 target modes: pseudo-orthogonality (left) and self-orthogonality (right)

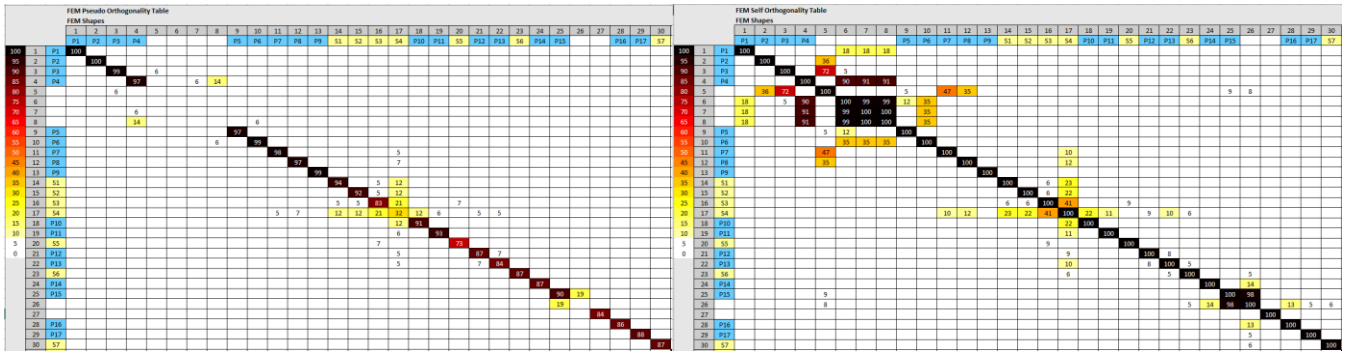

Figure 16. Artemis I DRT FEM first 30 modes that include the first 24 target modes: pseudo-orthogonality (left) and self-orthogonality (right)

The Artemis I DRT FEM was run through a "simulated" rollout using uncorrelated white noise force time histories applied at the bottom of the JEL's to simulate ground rollout forces. This simulation generated response acceleration time histories at all accelerometer locations, which were used to exercise post-test analysis tools and help the team develop familiarity with the FEM and the data prior to the Artemis I DRT rollout occurring.

DATA QUALITY CHECKS AND PREPROCESSING

Time-domain and frequency-domain data quality checks have always played an important role in traditional modal testing (i.e., EMA) to help ensure obtaining valid modal parameters. However, because OMA does not have measured input excitation into the system as EMA does, these data quality checks become more important and increased rigor should be applied when performing them. Skipping data quality checks can lead to corrupted time histories from which the OMA analysis can produce "reasonable looking" answers that are not valid. Hence, the temptation of rushing to perform any OMA (or EMA) analysis prior to completing rigorous data quality checks should be avoided [26].

The standard time-domain data quality checks should include inspecting time histories for data dropouts, underflow (i.e., digitization error), overflow (i.e., clipping), excessive low frequency signal drift, excessive skewness/asymmetries, excessive/unexpected excursions or transients, oscillation blooms (i.e., ringing), and other unexpected behaviors. This helps to identify bad/questionable channels and channels that may be able to be "corrected". Acceleration time histories that have overall amplitude levels that are out of family with expectedly similar acceleration time histories potentially indicates bad/questionable channels and channels that may be able to be "corrected". Scaling issues could be due to incorrect sensitivities entered into the DAQ channel table. Standard statistics (e.g., mean, max, min, standard deviation, kurtosis, and crest factor) should also be computed and reviewed. These time-domain data quality checks should be applied to both the raw unfiltered test data as well as the filtered test data that is ultimately used in the OMA analysis. While this helps to verify the health of the channels, it does not necessarily verify the as installed accelerometers are consistent with the channel table. A useful data quality check that helps to identify channel table errors is to take the acceleration time histories on the ML at the four ML/CT pickup points and apply them to the physical FEM. Comparison of the lowpass (LP) filtered test simulated and test measured acceleration time histories can quickly identify channel table errors, particularly polarity issues.

The standard frequency-domain data quality checks should include computing and comparing Power Spectral Densities (PSD's), also known as Auto Spectral Densities (ASD's) of channels that are expected to be in-family and identifying harmonic excitation due to CT Harmonics and rotating machinery operating in both the CT and ML Base, etc. These standard frequency-domain data quality checks should be applied to both the raw unfiltered time histories as well as the filtered time histories that are used in the OMA analysis in order to identify bad/questionable channels and channels that may be able to be "corrected". Again, while this helps to verify the health of the channels, it does not necessarily verify the as installed accelerometers are consistent with the channel table. PSD's were also inspected to see if they possessed distinct resonance peaks at the Artemis I DRT and WDR FEM modal frequencies, CT harmonics if the CT was moving, and 60 Hz harmonics due to electronic noise. These PSD's were also compared to the accelerometers manufacture's specified sensor noise floor PSD's to obtain a preliminary estimate of the Signal-to-Noise Ratio (SNR) on each channel. PSD waterfall plots were used in determining stationarity (i.e., time invariant behavior) and nonstationarity (e.g., transients, time dependent behavior, etc.) characteristics of each acceleration time history.

Low frequency signal drift, which is an artifact of the signal conditioning, can produce can have detrimental effects upon both the OMA time-domain and frequency-domain techniques. It can cause the OMA time-domain techniques to try and fit extraneous modes to them and the singular values can have misleading peaks. Unwanted high frequency content can have similar detrimental effects. Therefore, acceleration time histories should be bandpass (BP) filtered prior to being input into the OMA analysis to only include the frequency range of interest in order to focus the modal identification process and minimize the computational burden on the OMA software.

Filtering used in this analysis consisted of digital 4^{th} order Butterworth filters. Butterworth filters were chosen because of their monotonic magnitude characteristics. 4^{th} order was chosen to help ensure filter stability. To quadruple the steepness of the filter rollup and rolloff (i.e., obtain the performance of a higher order filter without the risk of having an unstable filter)

and to eliminate phase distortion, the time acceleration histories were passed forwards and backwards through this digital filter twice. However, keep in mind that while running time histories forwards and backwards through a digital filter multiple times increases the filter's performance (i.e., steepness of the rollup and rolloff), it comes at the cost of accentuating the filter transients at the beginning and ending of the time histories. If transients cannot be tolerated, butterflying techniques can be used on the acceleration time histories prior to filtering, which will eliminate transients at the beginning and ending of the bandpass filtered acceleration time histories. For this study, the transients had an insignificant duration with respect to the total duration so that excluding them did not impact the OMA analysis.

The validity (i.e., stability, performance, transient behavior) of any filter being used should be verified by inspection of the filtered time histories should be performed to identify any filtering transients that may occur at the beginning or ending of the filtered time histories. The left side of Figure 17 compares the unfiltered and BP filtered acceleration time histories, which shows the BP filtered acceleration time history has a filtering transient at its beginning. This BP filtered acceleration time history also had a filtering transient that occurring at its end. The filter validity should also be verified by comparing PSD's of the unfiltered and filtered time histories. The right figure of Figure 17 compares the PSD's of an unfiltered and BP filtered acceleration time histories. Note the PSD computed on the BP filtered acceleration time history excluded the transients at the beginning and end. This verified the validity of this BP filter.

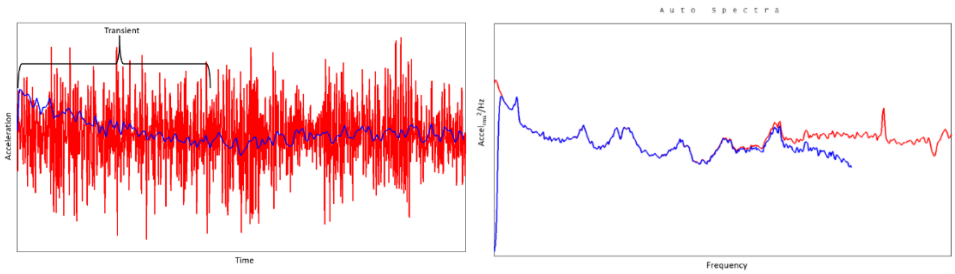

Figure 17. Acceleration time histories (left) and PSD comparison (right): unfiltered (red), BP filtered (blue)

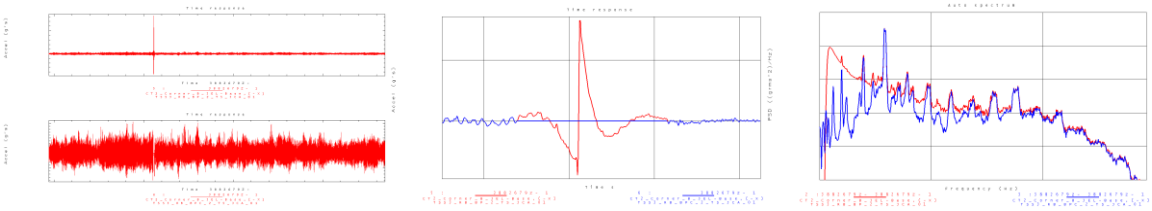

Figure 18. Acceleration time histories (left) with excursion (top) and with excursion removed (bottom), closeup view (center) with (red) and with excursion removed (blue), and PSD comparison (right): with excursion (red) and without excursion (blue)

As many channels as reasonably possible should be retained in the OMA analysis to retain as large a set of test DOF as possible, which helps to adequately identify all target modes (i.e., unique test shapes based upon a MAC or self-orthogonality criteria [45]). Time histories can have excursions due to such things as intermittent contact issues (i.e., sharp step followed by monotonic exponential decay), while others appeared to be true impulses generated by something or someone impacting the structure, personnel moving around on the ML, or cryogenic contraction (stick/slip). Channels having a limited number of excursions can be reasonably retained by manually removing their excursions either by zeroing out the range between the nearest "valid" time points or by linearly interpolating between them. Comparisons of the PSD's of the original time history and "corrected" time history having the excursions removed can be used to verify the excursion removal did not significantly alter the underlying dominant frequency content of the signal. The left and center figures in Figure 18 shows an example of where a very large amplitude excursion, which looked like it was caused by intermittent contact, has been removed by zeroing it out. The right figure in Figure 18 compares the PSD's of the original and "corrected" acceleration time histories. The presence of this excursion masked the true low frequency dynamics present in the acceleration time history and would

have negatively impacted the effectiveness of the OMA frequency-domain techniques (i.e., inaccurate mode shape coefficients for the low frequency target modes for this test DOF).

TIME SYNCHRONIZATION OF MDAS AND CTDAS DATA

Unfortunately, time stamping of data channels does not ensure they are adequately time synchronized. In adequate time synchronization results in cross spectral densities having erroneously large phase angle distortions, which results in the OMA identified test mode shapes having erroneously high complexity. With the ultimate goal of obtaining real valued OMA identified mode shapes, this phase angle distortion leads to the real portion of the complex valued OMA identified test mode shapes not well capturing the underlying dynamics. This will negatively impact any model correlation effort. Therefore, it is important that data channels be adequately time synchronized.

Both the MDAS and CTDAS had IRIG-B timing, however this did not provide sufficiently accurate time synchronization for OMA analysis. A common trigger signal was collected on both MDAS and CTDAS for post processing time synchronization, however, attempts to use it were not successful. Fortunately for the Artemis I DRT, there were MDAS triaxial accelerometers on the ML side of each of the four ML/CT pickup points and CTDAS triaxial accelerometers on the CT side. These pairs of MDAS and CTDAS triaxial accelerometers were spatially close enough together that over the frequency range of interest they had essentially the same acceleration time history (i.e., no relative motion) and could be used for time synchronization. The MDAS and CTDAS acceleration time histories were first LP filtered to remove frequency content that was significantly above the frequency range of the target modes. This helped to visually identify common dominant low frequency events in both, which could be used to estimate the time shift between them. Without LP filtering these pairs of MDAS and CTDAS accelerometers have significant relative motion at higher frequencies, which would not allow them to be time synchronized. Visually inspecting the pairs of MDAS and CTDAS acceleration time histories showed the MDAS and CTDAS clocks during Artemis I DRT rollout differed by about 1 minute at times and 2 minutes at other times. It is unknown why the relative timing difference was not constant. During Artemis I DRT rollback their clocks differed by an approximately consistent 17 sec. Based upon these clock differences, the lag window used to compute the cross-covariances was determined. Note that the cross-covariance function was used instead of the cross-correlation function in order to eliminate the impact of either the MDAS or CTDAS acceleration time histories having low frequency signal drift, which would result in them having nonzero means over the lag window they were analyzed. Figure 19 shows the same two events in the MDAS and CTDAS acceleration time histories at CT Corner A ML/CT pickup points, which indicates the MDAS and CTDAS clocks differed by approximately 54 sec.

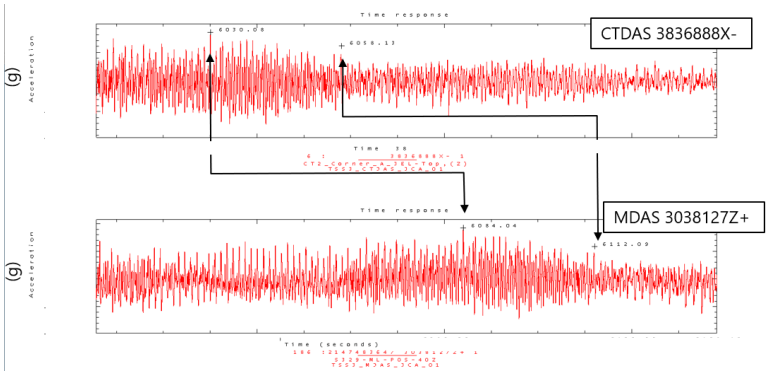

Figure 19. Comparison of CT Corner A ML/CT pick up point acceleration time histories: CTDAS (top) and MDAS (bottom)

These acceleration time histories, which had already been LP filtered, were upsampled to a higher sampling frequency based upon the desired maximum absolute phase angle error at the highest frequency of interest (e.g., if a maximum absolute phase angle of error of 0.5 deg at 20 Hz was desired then the upsampling frequency would need to be at least 14.4 kHz). Care needs to be taken to minimize high amplitude high frequency artifacts that the upsampling process introduces. Figure 20 shows two methods of upsampling with the method shown on left introducing significantly higher amplitude high frequency artifacts than the method on the right.

The left figure in Figure 21 shows the cross-covariance computed on this pair of upsampled MDAS and CTDAS acceleration time histories and the peak in the cross-covariance that occurs around 54 seconds. The time steps the cross-covarions peak occurred at was determined and used to precisely time shift the MDAS and CTDAS acceleration time histories. This time synchronization was verified by computing the cross covariance on these time synchronized MDAS and CTDAS acceleration time histories, which is shown in the right figure in Figure 21. The cross-covariance peak occurred at 0 sec time lag (i.e., 0 time steps) as shown in the right figure in Figure 21, which verifies time synchronization has been achieved.

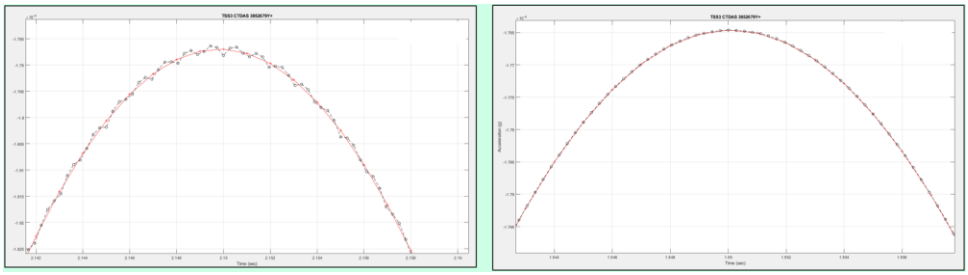

Figure 20. Comparison of two upsampling techniques: more artificial high frequency artifacts (left) and less (right)

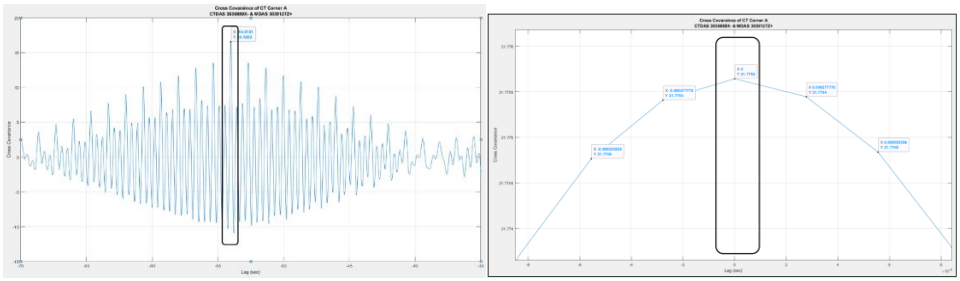

Figure 21. Cross covariance of the MDAS and CTDAS acceleration time histories: before time synchronization (left) and after time synchronization (right).

The time synchronized MDAS and CTDAS acceleration time histories were then down sampled to the desired slower sampling frequency and HP filtered to remove any low frequency signal drift. Finally, the time synchronized BP filtered MDAS and CTDAS acceleration time histories were overlaid as the final check of their time synchronization. This final check was performed on all other pairs of the ML/CT pickup point MDAS and CTDAS time synchronized BP filtered acceleration time histories. Because the ground wind direction and wind speed time histories were only used to assess vortex shedding frequencies, it was adequate to roughly time synchronized them using just the MDAS and SDAS clocks.

OMA ANALYSIS

OMA analysis was performed on both the Artemis I DRT Rollout and Rollback time segments, which included time intervals when the CT was stopped, traveling at nearly constant speeds, and the CT speed was varying. OMA analysis was performed on one WDR time segment where SLS was partially fueled. The WDR data collected when the SLS was partially fueled is the only modal data collected on Artemis I with the Core Stage in a fueled state (the Artemis I IMT had the Core Stage empty) and thus provides important supplemental information.

Investigations into the best set of projection channels for the Artemis I WDR was performed. The left figure in Figure 22 shows 3 Projection Channels automatically selected by the OMA software, which consisted of three horizontal test DOF with one at the top of Artemis I, one on the Right Booster, and one at an upper level of the ML Tower. Manual selection of Projection Channels was used to determine if the Projection Channels could be improved upon. The manual selection was based upon visual inspection of the FEM target modes and not wanting Projection Channels of test DOF near the CT Trucks to try and minimize the effects of the CT harmonics. Also, the ISVV-010 and Partial Stack OMA analysis showed that Projection Channels including test DOF at the top of the ML Tower, Artemis I, and in the mid span of the boosters should be

considered [11]. Vertical test DOF on the ML Base Deck 0 and on Artemis I were assessed as potential Projection Channels, but were found not to be needed. Also, the vertical accelerations on Artemis I and the ML Base showed significant response due to the CT harmonics. Nine projection channels were chosen for the Artemis I WDR, which include horizontal test DOF near the top of Artemis I (i.e., near the Launch Abort System (LAS)), horizontal test DOF near the midspan of each booster, and a horizontal test DOF on the Core Stage at the right booster forward attachment point. The right figure in Figure 22 shows this final set of nine Artemis I WDR Projection Channels. This set of nine Projection Channels also proved to be adequate for the Artemis I DRT.

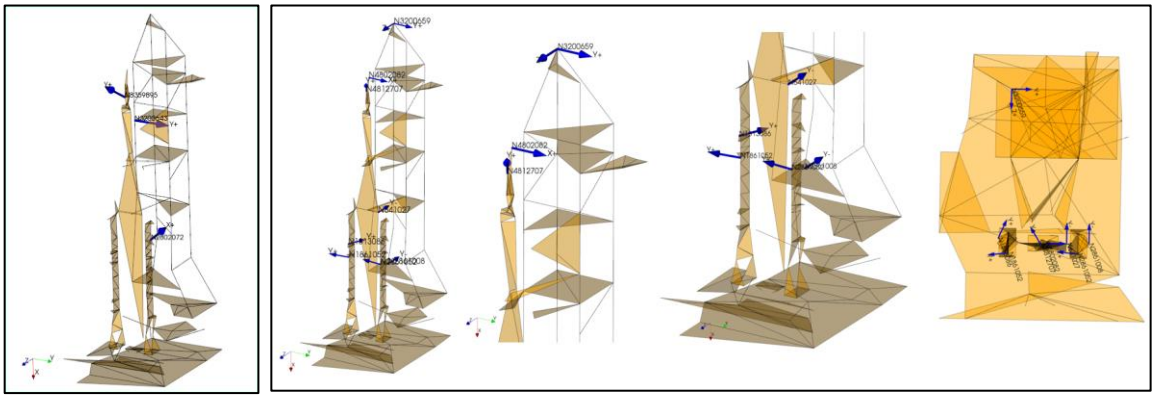

Figure 22. Artemis I WDR projection channels: 3 automatically selected (left) and final 9 (right)

Accurate CT speed is needed to accurately estimate the CT Truck harmonic frequencies to help inform which OMA identified modes have a high likelihood of being due to a CT harmonic instead of a true structural mode. When the CT speed is constant, the most accurate estimate of CT speed is obtained by comparing the CT speed time history PSD peak frequencies to those of the CT harmonic frequencies.

Similarly, ground wind speed and direction are needed to estimate vortex shedding frequencies of the cylindrical structures that make up Artemis I (i.e., the MPCV Orion SM, SLS Core Stage, SLS Boosters) to help inform which OMA identified modes have a high likelihood of being due to vortex shedding instead of a true structural mode. 60 second moving averages were computed on the ground wind direction and ground wind speed time histories to better understand the steady-state wind conditions. Note that when the ground wind direction is shown to be oscillating between 0 deg and 360 deg, it is actually oscillating about 0 deg. Hence the 60 sec moving average of the wind direction, when this is happening, is not accurate and has no meaning. For both the Artemis I DRT and WDR the steady state ground winds were relatively light, and the vortex shedding frequencies were below the frequency range of the target modes. The left and right figures in Figure 23 show the ground wind direction and ground wind speed for Artemis I DRT Rollout and Rollback, respectively.

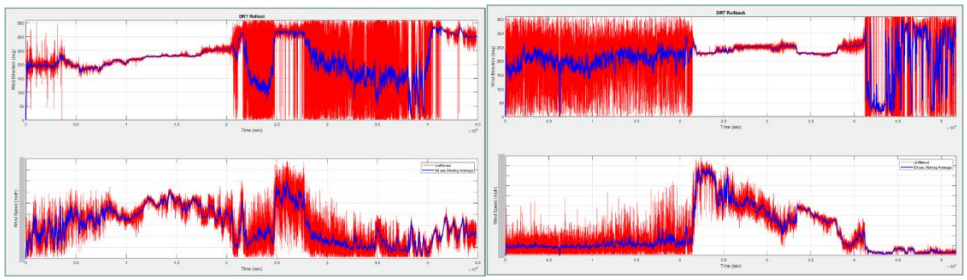

Figure 23. Artemis I DRT rollout (left) and rollback (right): ground wind direction (top) and wind speed (bottom): unfiltered (red) and 60 sec moving average (blue)

As with the OMA analysis of the ISVV-010 rollout, multiple OMA mode identification techniques were required to identify all target modes [11]. OMA analysis started with the time-domain Stochastic Subspace Identification Extended Unweighted Principal Component (SSI-UPCX) technique. Relaxing the SSI-UPCX parameters was done to and obtain more modes

corresponding to dominant SVD peaks. However, care needed to be exercised to prevent obtaining unrealistic modal damping values, overly complex mode shapes, and poor quality mode shapes. Next, the Curve Fitting Frequency Domain (CFDD) technique was used to verify the SSI-UPCX identified modes and was used judiciously to identify additional modes corresponding to dominant singular value peaks, which had positive modal damping, that the SSI-UPCX technique had missed. Then, the Enhanced Frequency Domain Decomposition (EFDD) technique was used to verify the SSI-UPCX and CFDD identified modes and used judiciously to identify additional modes corresponding to dominant singular value peaks, which had positive modal damping that the SSI-UPCX and CFDD techniques had missed. Finally, the Frequency Domain Decomposition (FDD) technique was used to verify the SSI-UPCX, CFDD, and EFDD identified modes and to identify modes for dominant singular value peaks not already captured, whether they were believed to be due to CT harmonics or not. Figure 24 and Figure 25 show the OMA analysis of the acceleration time histories of the Artemis I DRT Rollback TSS3 bandpass filtered acceleration time histories when the CT was moving at a constant speed. The left figure in Figure 24 shows the SSI-UPCX stabilization diagram, which has a well-developed racetrack pattern of the pole estimates corresponding to many of the dominant singular value peaks. The right figure in Figure 24 shows the CFDD fit to one of the dominant singular value peaks. The left figure in Figure 25 shows the EFDD fit to one of the dominant singular value peaks. The right figure in Figure 25 shows the FDD fit to one of the singular value peaks, which had not had a mode identified for it by either the SSU-UPCX, CFDD, or EFDD techniques.

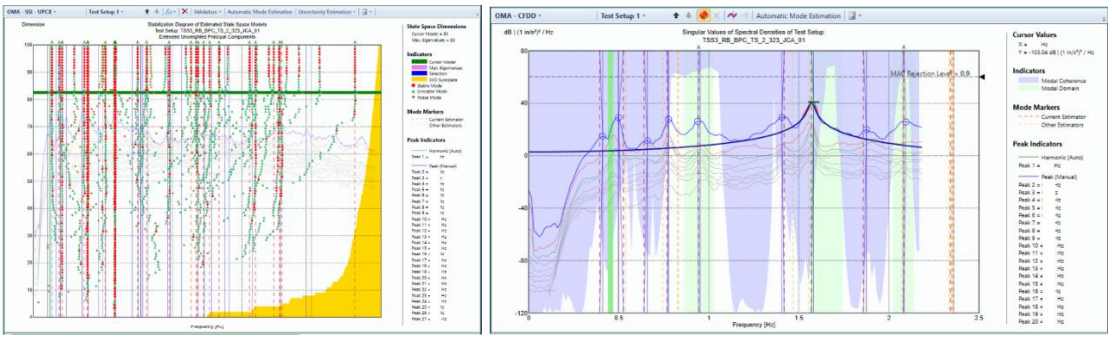

Figure 24. Artemis I DRT rollback TSS3, CT moving at constant speed: SSI-UPCX stability diagram (left) and CFDD (right)

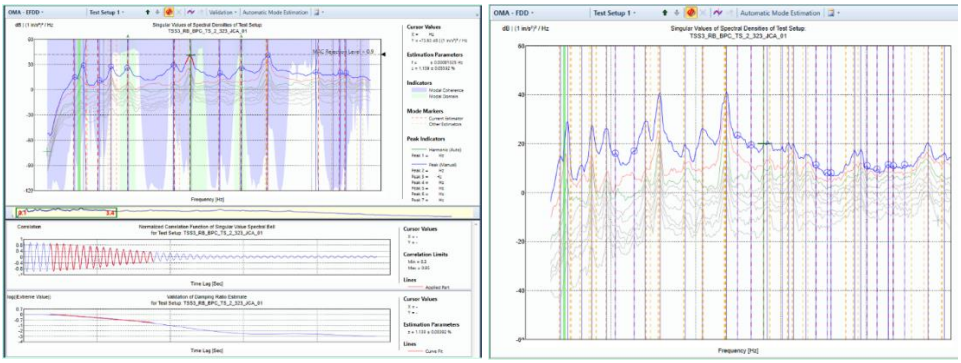

Figure 25. Artemis I DRT rollback TSS3, CT moving at a constant speed: EFDD (left) and FDD (right)

A FEM having a symmetric positive definite mass matrix M and a symmetric positive semidefinite stiffness matrix K has real valued mode shapes Φ that are orthogonal to the mass and stiffness matrix (i.e., $\Phi^{\mathrm{T}}M\Phi$ and $\Phi^{\mathrm{T}}K\Phi$ are diagonal matrices). If these real valued mode shapes are normalized so that $\Phi^{\mathrm{T}}M\Phi$ is the identity matrix, then $\Phi^{\mathrm{T}}K\Phi$ is a diagonal matrix with the square of the modal frequencies in units of rad/sec on its diagonal and these modes are called real normal modes. If a FEM having a symmetric positive definite mass matrix M, a symmetric positive semidefinite damping matrix C, and a symmetric positive semidefinite stiffness matrix K has complex valued mode shapes Ψ, these complex valued mode shapes are not orthogonal with respect to M, C, or K (e.g., $\Psi^{T}M\Psi \neq$ diagonal matrix) [27]. Therefore, the self-orthogonality (ORTHO) and cross-orthogonality (ORTHO) are not valid criteria for comparisons of these complex valued mode shapes. Note that the self

Modal Assurance Criteria (MAC) and cross Modal Assurance Criteria (XMAC) remains a valid comparisons of complex valued mode shapes.

Real valued test mode shapes that "best" approximate the complex valued OMA mode shapes are required for correlating to the Artemis I DRT and WDR FEM's, which have real normal modes. This was achieved by normalizing the complex valued OMA mode shapes by rotating them (i.e., multiplied by $e^{j\theta}$) to "best" lie on the real axis in a least-squares sense. The left figure in Figure 26 shows the unnormalized complex valued OMA mode shape and the right figure shows the normalized complex valued OMA mode shape. It can be seen the unnormalized complex valued OMA mode shape was rotated clockwise approximately 55 degrees (i.e., multiplied by $e^{j\theta}$, where $\theta \approx -(55\text{deg})(2\pi \text{ rad}/360\text{deg}) = -0.96$ rad) to "best" lie on the real axis. Then the real portion of these normalized complex valued OMA mode shapes were taken to obtain real valued OMA mode shapes. Finally, these real valued OMA mode shapes were then back expanded to have all three translational DOF at each accelerometer location using the Artemis I DRT or WDR TAM's and animated using the TDM for visual interpretation.

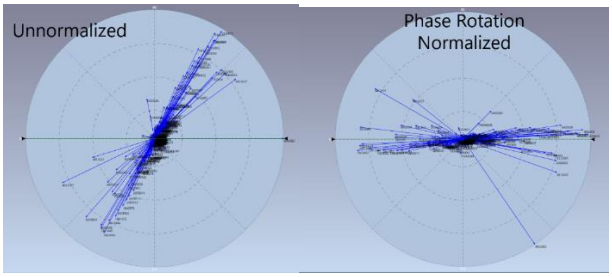

Figure 26. Complex valued mode shape: unnormalized (left) and normalized (right)

For each time interval analyzed, the XMAC and XORTHO were used to compare the real valued OMA mode shapes identified by each OMA technique and normalized as discussed above. Mode shapes were considered equivalent if their XORTHO value was ≥ 0.9 and their modal frequency difference was less than 0.1 Hz or +/- 5%, which was based upon NASA-STD-5002a criteria [25]. From these XORTHO comparisons, a preliminary final mode set from each time interval analyzed was constructed with a confidence assigned to each OMA mode based upon the number of OMA techniques that identified it. Figure 27 shows the first 13 OMA modes of a total of 57 OMA modes identified during the Artemis I DRT rollback when the CT was moving at a nearly constant speed (TSS3_RB_2). Most modes have either low confidence or very low confidence. Modes suspected of being due to CT harmonics highlighted in red.

= High Confidence Mode (i.e. identified by SSI-UPCX, CDFF, and EFDD methods).
= Medium Confidence Mode (i.e. identified by both CFDD and EFDD methods).
= Low Confidence Mode (i.e. only identified by CFDD, EFDD, or SSI-UPCX method).
= Very Low Confidence Mode (i.e. only identified by FDD method).
= Suspected CT Harmonic

Number of high confidence modes =	4
Number of medium confidence modes =	8
Number of low confidence modes =	18
Number of very low confidence modes =	15
CT Harmonics =	12
Total number of modes =	57

Preliminary Final Mode Set

Mode #	Method	Freq (Hz)	Mode Shape Desciription	SSI-UPCX Freq (Hz)	CFDD Freq (Hz)	EFDD Freq (Hz)	FDD Freq (Hz)
1	CFDD	1	ML Deck Bending, ML Tower & SLS 1st Lateral Bending Z-Axis.	NF	1.00	1.00	NF
2	EFDD	1.32	ML Deck Rotation About Z-Axis, ML Tower & SLS 1st Lateral Bending Y-Axis.	0.538	1.33	0.523	NF
3	CFDD	1.62	ML Tower & SLS 1st Lateral Bending Y-Axis Out-of-Phase, ML Tower & SLS 1st Torsion In-Phase.	NF	1.62	1.62	NF
4	SSI-UPCX	1.88	ML Deck Z-Axis Translation, ML Tower 1st Lateral Bending Y-Axis & Z-Axis, SLS 1st Lateral Bending Y-Axis & Z-Axis.	0.744	NF	NF	NF
5	CFDD	1.94	Large Amount Of ML Deck Z-Axis Translation, ML Tower 1st Lateral Bending Y-Axis & Z-Axis, SLS 1st Lateral Bending Y-Axis & Z-Axis.	NF	1.94	1.96	
6	SSI-UPCX	2.09	ML Deck Z-Axis Translation, ML Tower & SLS 1st Lateral Bending Z-Axis Out-of-Phase.	0.83	NF	NF	NF
7	CFDD	2.39	ML Deck Z-Axis Translation, ML Tower & SLS 1st Lateral Bending Z-Axis Out-of-Phase.	NF	2.39	2.39	NF
8	FDD	2.67	ML Deck Z-Axis Translation, SLS 1st Lateral Bending Z-Axis.	NF	NF	NF	2.67
9	FDD	3.23	ML Deck Z-Axis Translation, SLS 1st Lateral Bending Z-Axis.	NF	NF	NF	3.23
10	EFDD	3.58	SLS 1st Lateral Bending Z-Axis.	NF	3.59	3.58	NF
11	SSI-UPCX	3.71	ML Deck Z-Axis Translation, ML Tower & SLS 1st Lateral Bending Z-Axis Out-of-Phase.	3.71	NF	NF	NF
12	SSI-UPCX	3.94	ML Deck Z-Axis Translation, ML Tower 1st Torsion, SLS 1st Lateral Bending Y-Axis Out-of-Phase, Boosters 1st Lateral Bending Y-Axis Out-of-	3.94	NF	NF	NF
13	CFDD	3.97	ML Deck Z-Axis Translation, ML Tower & SLS 1st Lateral Bending Z-Axis Out-of-Phase.	3.98	3.97	3.98	NF

Figure 27. Preliminary final OMA mode set of Artemis I DRT rollback when the CT moving at a constant speed (Modes 1 – 13 only) (normalized to lowest frequency mode)

Figure 28 shows the XORTHO of FEM target modes and the real valued OMA mode shapes showing there are significant differences between them except for the first three modes. The mode comparison table shows the cumulative root sum square (CRSS) of each of the real valued OMA mode shapes with respect to all FEM target mode shapes is close to or at 100%. This indicates all real valued OMA mode shapes are within the vector space of the FEM target mode shapes (i.e., the real valued OMA mode shapes can be well approximated by a linear combination of the FEM target mode shapes). Not shown, the CRSS of each FEM target mode shape with respect to all real valued OMA mode shapes is also close to or at 100%, which indicates all FEM target mode shapes are within the vector space of the real valued OMA mode shapes. This collectively shows that OMA analysis had identified all FEM target mode dynamics.

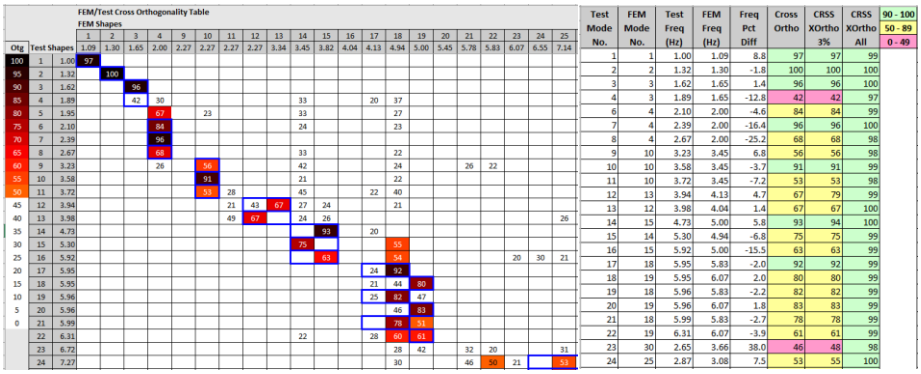

Figure 28. Artemis I DRT FEM vs Preliminary final OMA mode set of Artemis I DRT rollback when the CT moving at a constant speed (Modes 1 – 24 only) (normalized to lowest frequency test mode): XORTHO (left) and mode comparison table (right)

The preliminary final mode set identified during the Artemis I DRT rollback when the CT was moving at a nearly constant speed (TSS3_RB_2) was combined with those identified during the Artemis I DRT rollback when the CT stopped (TSS3_RB_1), and those identified when the CT was moving at a different nearly constant speed (TSS5_RB_1). The ORTHO of the first 27 modes of this combined OMA preliminary final mode sets is shown in Figure 29. Modes that were within 0.1 Hz or 5% modal frequency and had ORTHO off-diagonal values ≥ 0.90 were judged to be the same mode. The similarity between these modes only holds for a few of the lowest frequency OMA modes, even though the OMA mode shapes look very similar. This indicates Artemis I DRT configuration has nonlinear characteristics since the OMA modes are dependent upon the CT speed.

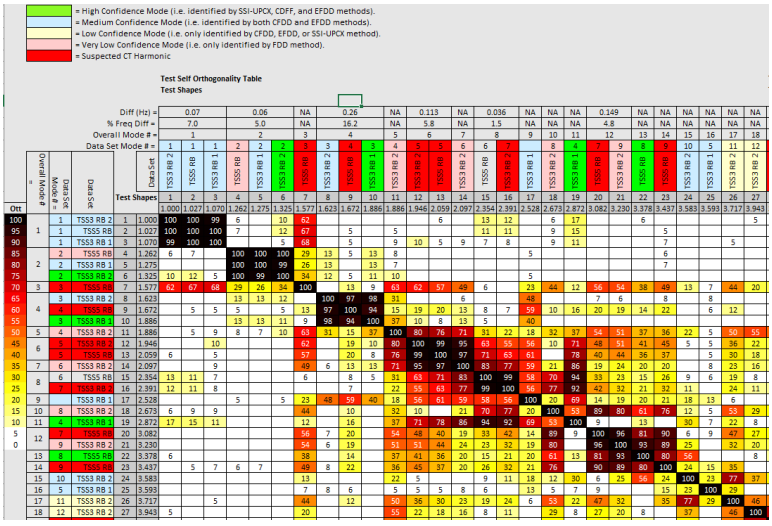

Figure 29. Combined OMA preliminary final mode sets (normalized to lowest test frequency mode)

CONCLUSION

OMA techniques will not replace traditional modal testing (i.e., EMA), but can provide important supplemental information and insights into the structural dynamics of hardware in its operational environment. CT harmonics, which lie within the frequency range of the fundamental target modes, manifest themselves as narrowband Gaussian random processes continue to be a significant challenge when applying OMA analysis to rollout data because they are difficult to analytically remove. Artemis I DRT and WDR configurations displayed nonlinear characteristics, which were dependent upon the CT and ground wind speeds. OMA techniques were successfully applied to the Artemis I DRT and WDR data for identifying preliminary final sets of modes that captured all Artemis I DRT and WDR FEM target mode dynamics, respectively. By applying OMA techniques to time intervals that have the CT moving at different, but nearly constant speeds, which shifts the CT harmonics, it is possible to compare the OMA modes from these different sets to identify true structural modes. However, the challenge is that due to the nonlinearity of Artemis I DRT configuration, the true structural modes from each of these time intervals can be significantly different, with the differences increasing with increasing frequency. Further work is needed to look at comparing OMA modes of selected components of the Artemis I DRT configuration (e.g., excluding umbilicals) to determine what is causing the differences in the OMA mode shapes and obtain a final complete mode set of OMA modes.

OMA analysis of the Artemis I DRT and WDR has also provided invaluable insights into what to expect during a possible Artemis IV DRT. Artemis IV will use the larger and more powerful SLS Block 1B launch vehicle and be integrated on and launch from the larger ML-2. This will lead to the Artemis IV DRT target modes having lower frequencies and a higher modal density than that of Artemis I DRT. Hence OMA analysis of the Artemis IV DRT will be more challenging than that of Artemis I DRT and require careful planning and execution to help ensure success.

ACKNOWLEDGEMENTS

The authors would like to thank the NASA Engineering Safety Center (NESC) for funding this work and the support and collaboration of MSFC EV31 Structural Dynamics & Integration Branch, MSFC ET40 Structural Dynamics Test Branch, and KSC NE-X Exploration Systems & Operations. Specific individuals that played key roles were Dan Lazor (MSFC-EV31) and Felipe Mora (MSFC-ET40) who provided test data, models, and data interpretation. Christopher Brown (KSC-NEXY0) and Kevin Decker (KSC NEXI0) who provided information on the ML and CT. Lance Proctor (LaRC-D206), Katachia Fields (MSFC-EV31), and Jonathan Band (MSFC-EV31) who provided valuable insights with respect to the models. Finally, the NESC is very grateful for the mentoring and guidance provided by Carlos Ventura Professor of Civil Engineering, University of British Columbia, in the theory and application of OMA techniques [28, 29].

REFERENCES

[1] James, G., et al, "Development of a Refined Space Vehicle Rollout Forcing Function", *Proceedings of the AIAA SciTech Conference 2016*, NTRS 20160014516.pdf.

[2] James, G., Grady, R. Allen, M., Bruno, E., "Forcing Function Estimation for Space System Rollout." *Proceedings of the 38th International Modal Analysis conference*, 2020.

[3] Elliot, K., James, G., Buehrle, R., Richart, J., "Space Shuttle Transportation (Roll-Out) Loads Diagnostics." *Proceedings of the 23rd International Modal analysis Conference*, 2005. NTRS 20050081824.pdf

[4] James, G., Carne, T, Elliot, K., Wilson, B., "Estimation Of The Space Shuttle Rollout Forcing Function," *Proceedings of the 23rd International Modal Analysis Conference*, 2005, NTRS 20060012130.pdf.

[5] Meyer, K., Nerolich, S., Burton, R., Gosselin, A., "Space Shuttle Crawler Transporter Vibration Analysis in Support of Rollout Fatigue Load Spectra Verification Program." *Proceedings of the 11th International Conference on Sound and Vibration*, 2004. NTRS 20120003345.pdf.

[6] "SLS Fact Sheet.", https://www.nasa.gov/exploration/systems/sls/factsheets.html.

[7] "NASA Facts: Space Launch System.", https://www.nasa.gov/sites/default/ files/files/SLS-Fact-Sheet_aug2014-finalv3.pdf.

[8] "SLS Rollout, NASA's Most Powerful Rocket Ever", https://www.youtube.com/watch?v=B_9wtpu8fcI, NASASpaceflight.com video of the Artemis I DRT Rollout, iCPSU oscillations occur at 2:57:37 elapse time.

[9] Akers, J., Sills, J., "Space Launch System Mobile Launcher Modal Pretest Analysis", *Proceedings of the 38th International Modal Analysis Conference*, 2020. NASA Technical Reports Server (NTRS) 20200000863.pdf.
[10] Stasiunas, E., Parks, R., Sontag, B., Chandler, D., "Modal Test of the NASA Mobile Launcher at Kennedy Space Center." Proceedings of the 38th International Modal Analysis conference, 2020. NTRS 20200001728.pdf.
[11] Akers, J., Sills, J., "Operational Modal Analysis of the Space Launch System Mobile Launcher on the Crawler Transporter ISVV-010 Rollout," *Proceedings of the 39th International Modal Analysis Conference*, 2021. NTRS 10598_ake.docx.
[12] Sills, J. and Allen, M., "Historical Review of 'Building Block Approach' in Validation for Human Space Flight." *Proceedings of the 37th International Modal Analysis Conference*, 2019.
[13] Honeycutt, J., Blevins, J., Cobb, S., Bryan, W., "NASA's Space Launch System Successfully Launches Artemis I Mission and Hardware Progress Continues for Next Artemis Missions", AIAA SciTech January 2023, NTRS Final - SciTech 2023 Abstract.pdf.
[14] Sills, J., "Multidisciplinary Dynamic Testing Challenges in Validating the NASA Artemis Architecture", 13th Annual Congress AICE, October 2020, NTRS AICE - Keynote Multidiscplinary_Final.pdf.
[15] "Mobile Launcher, NASA Fact Sheet." https://www.nasa.gov/sites/default/files/atoms/files/mobilelauncher_factsheet_v2.pdf.
[16] "Mobile Launcher Umbilicals and Support, NASA Facts." https://www.nasa.gov/sites/default/files/atoms/files/ml_umbilicals20160523.pdf.
[17] Crawler-Transporters, NASA Fact Sheet.", https://www.nasa.gov/sites/default/files/638823main_crawler-transporter.pdf.
[18] "Crawler-Transporter 2, NASA Fact Sheet." https://www.nasa.gov/sites/default/files/atoms/files/crawler-transporter2_factsheet_508compliant.pdf.
[19] "Crawler-transporter", https://en.wikipedia.org/wiki/Crawler-transporter.
[20] "Upgrades Will Prepare Crawlerway for Space Launch system," https://www.nasa.gov/exploration/systems/ground/crawlerway_upgrades.html.
[21] Buehrle, R., Kappus, K., "Operating Deflection Shapes for the Space Shuttle Partial Stack Rollout." *Proceedings of the 23rd International Modal analysis Conference*, 2005. NTRS 20050081825.pdf
[22] "Shuttle Liftoff Require Precision Launch Pad", https://www.nasa.gov/mission_pages/shuttle/flyout/launchpadflyout.html
[23] "Behind the Rollout", https://www.nasa.gov/mission_pages/shuttle/flyout/rollout.html
[24] "Rotating Service Structure (RSS)", https://www.nasa.gov/mission_pages/shuttle/launch/rotating-service-structure.html
[25] NASA-STD-5002a*: Load Analyses Of Spacecraft And Payloads*, Section 4.9.1.8 through 4.9.1.11, September 25, 2019, https://standards.nasa.gov/sites/default/files/standards/NASA/A/0/nasa-std-5002a.pdf.
[26] Akers, J., Otten, K., Sills, J., Larsen, C., "Modern Modal Testing: A Cautionary Tale", *Proceedings of the 37th International Modal Analysis Conference*, 2019, NTRS 20190001554.pdf.
[27] D. J. Ewins, MODAL Testing: Theory, Practice, and Application, 2nd ed, RSP, England, 2000.
[28] Brinker, R., Ventura, C., Introduction to OPERATIONAL MODAL ANALYSIS, Wiley, New York, 2015.
[29] Andersen, P., Ventura, C., "Operational Modal Analysis: Background, Theory & Practice.", *39th International Modal Analysis conference preconference course*, 2020.